Automated Extraction and Variability Analysis of Sulcal Neuroanatomy

Georges Le Goualher,* Emmanuel Procyk, D. Louis Collins, Raghu Venugopal, Christian Barillot, and Alan C. Evans

***Abstract*— Systematic mapping of the variability in cortical sulcal anatomy is an area of increasing interest which presents numerous methodological challenges. To address these issues, we have implemented sulcal extraction and assisted labeling (SEAL) to automatically extract the two-dimensional (2-D) surface ribbons that represent the median axis of cerebral sulci and to neuroanatomically label these entities.**

To encode the extracted three-dimensional (3-D) cortical sulcal schematic topography (CSST) we define a relational graph structure composed of two main features: vertices (representing sulci) and arcs (representing the relationships between sulci). Vertices contain a parametric representation of the surface ribbon buried within the sulcus. Points on this surface are expressed in stereotaxic coordinates (i.e., with respect to a standardized brain coordinate system). For each of these vertices, we store length, depth, and orientation as well as anatomical attributes (e.g., hemisphere, lobe, sulcus type, etc.). Each arc stores the 3-D location of the junction between sulci as well as a list of its connecting sulci.

Sulcal labeling is performed semiautomatically by selecting a sulcal entity in the CSST and selecting from a menu of candidate sulcus names. In order to help the user in the labeling task, the menu is restricted to the most likely candidates by using priors for the expected sulcal spatial distribution. These priors, i.e., sulcal probabilistic maps, were created from the spatial distribution of 34 sulci traced manually on 36 different subjects. Given these spatial probability maps, the user is provided with the likelihood that the selected entity belongs to a particular sulcus.

The cortical structure representation obtained by SEAL is suitable to extract statistical information about both the spatial and the structural composition of the cerebral cortical topography. This methodology allows for the iterative construction of a successively more complete statistical models of the cerebral topography containing spatial distributions of the most important structures, their morphometrics, and their structural components.

***Index Terms*—Active model, cerebral cortex, MRI, probabilistic atlas, sulci.**

Manuscript received April 20, 1998; revised September 29, 1998. This work was supported in part by the Regional Council of Brittany, France and by the HBMP funded International Consortium for Brain Mapping. The Associate Editor responsible for coordinating the review of this paper and recommending its publication was V. Johnson. *Asterisk indicates corresponding author.*

*G. Le Goualher, D. L. Collins, and A. C. Evans are with the McConnell Brain Imaging Center and the Department of Neurology and Neurosurgery, Montreal Neurological Institute and Hospital, McGill University, Montreal, PQ, Canada (e-mail: georges@bic.mni.mcgill.ca).

E. Procyk was with the McConnell Brain Imaging Center and the Department of Neurology and Neurosurgery, Montreal Neurological Institute and Hospital, McGill University, Montreal, PQ, Canada. He is now with INSERM U94, 69500 Bron, France.

R. Venugopal is with the McConnell Brain Imaging Center, Montreal Neurological Institute and Hospital, McGill University, Montreal, PQ, Canada.

C. Barillot was with the Laboratoire Signaux et Images en Médecine, Université de Rennes I, France. He is now with the French National Research Institute for Research in Computer Science and Control (IRISA), VISTA project, Rennes, France.

Publisher Item Identifier S 0278-0062(99)04004-5.

I. Introduction

CEREBRAL sulci form macroscopic anatomical landmarks on the surface of the brain. Several studies [1]–[3] have suggested that some major functional areas can be located with respect to these *anatomical landmarks* (i.e., an *anatomo-functional correlation* exists). Nevertheless, the knowledge of this relationship is poorly understood at present in part because of inconsistent strategies employed for tracing cortical features such as gyri and sulci. In order to supplement this information, a systematic means of representing and quantifying the cerebral cortex is needed (the reader is referred to Ono's atlas as a descriptive or semiquantitative attempt to capture the sulcal variability [4]). In particular, detecting and matching a set of generic cortical landmarks between subjects will allow for intersubject comparisons.

The main difficulty when establishing this anatomical map comes from the high intersubject variability of the cortical topography. More precisely, one can denote shape variability (highlighted by variability in morphometrical parameters) as well as structural variability of the cortical topography (sulcus' body interruption, free supplementary sulci). This structural variability is the main problem when dealing with sulcus recognition and makes the definition of a common standard nomenclature to describe the cortical topography a very tedious task. In fact, there is only interexpert agreement on the nomenclature and identification of the main sulci (central sulcus, sylvian fissure, ...). Secondary and tertiary sulcal patterns are described in many different and mutually incompatible ways. Even for the major landmarks, ending boundaries are rarely defined, which leads to considerable subjectivity when computing certain statistics such as sulcal length.

Only the observation and the recovery of statistical parameters representing the normal variability of the sulci allow for the definition of objective criteria for the recognition or the comparison of these anatomical structures. Therefore, an atlas of the cerebral sulci must contain a set of statistical parameters useful for an objective structural description. This atlas must contain morphometrics (mean length, mean depth of a sulcus, the standard deviation of these measures, but also other shape parameters), data dealing with the spatial location of the anatomical structures (probability maps expressed in a common referential frame) and statistical information about the occurrence of the different sulcal patterns (number of folds which compose a sulcus, frequencies of connection between two sulci, etc., ...).

In the first part of this paper, we present a method to extract and to represent the cortical topography (composed

of a set of folds and the possible connections between these elements) from *in vivo* observations obtained through three-dimensional magnetic resonance imaging (3-D MRI). This information is encoded in a graph structure. Vertices of the graph represent the cortical folds (one or several folds may constitute a cerebral sulcus as defined by an anatomist), arcs represent the connections between these entities. We simplify the structure of a cortical fold by modeling its median surface. Our method (*the active ribbon*) allows us to extract a parametric representation of this median surface [5]. This parametric representation is suitable both for visualization purposes and for the computation of morphometric parameters.

We show that our sulcal topography representation is reliable and suitable to extract statistical information from a set of labeled graphs. In MRI data obtained from 20 individuals, we study the accuracy of our shape modeling method, we compute sulcus morphometric parameters and compare probability maps obtained manually and semiautomatically with the active ribbon method.

The last part of this paper presents how SEAL (sulcus extraction and assisted labeling) assists the user in the labeling task by presenting the most likely candidate names for each fold by using spatial priors for sulcal distribution. These priors, i.e., sulcal probabilistic maps, were created from the spatial distribution of 34 sulci traced manually on 36 different subjects.

II. Background

Several neuroanatomical studies have been conducted to determine, from a set of observations, *morphometrics* associated with the main sulci [6], [7], spatial distributions of these landmarks [8], [9], or the most likely *structural decompositions* of these entities [4]. This set of observations and retrieved statistics are still insufficient or hardly usable. One can note in particular that many of these measurements have been realized with *post mortem* subjects which can differ in shape from *in vivo* observations. On the other hand, the measures that are generally used only capture part of the morphological variability. Another major limitation is the small number of samples generally used to compute statistics representing spatial distributions of the anatomical structures. Classical atlases of the human brain and other species have been derived from a single brain, or brains from a very small number of subjects [10]. By taking advantage of current MRI technology which accurately represents *in vivo* cortical anatomy, a detailed sulcal description and representation from a large number of subjects can be integrated in the definition of electronic brain atlases giving more precise neuroanatomical information than ever before possible.

In many studies of *morphometrics* only gross measurements such as sulcus length and depth have been used. These parameters are then used to find, for example, significant differences between subgroups and more generally to define a standard anatomy. Other shape parameters, describing more subtle interindividual shape deformations, have also been introduced in the literature [11]–[13] but not yet introduced into published atlases. The reason for this is that the computation of such parameters relies on previously unavailable shape modeling techniques.

When studying the *spatial distribution* of brain structures, a common referential frame is needed to express, compare, and share data. The principles of proportional scaling defined by Talairach [14] has been accepted and is used by much of the neurological imaging community as a common brain-based coordinate system. Nevertheless, the linear proportional scaling method introduced in this atlas does not account for highly variable portions of the cerebral cortex (e.g., neocortex and peri-sylvian zones). This simple proportional scaling method has been extended through various image deformation paradigms [15]–[19]. While these approaches also apply for automatic indentification of brain's structure, the considerable intersubject structural variability of the cerebral cortex topography is still not sufficiently well-modeled to allow accurate labeling of individual sulci [20]. Nevertheless, compensation of local anatomical differences through these methods allows more compact spatial distributions in the location of most anatomical entities [21]. Specific referential frames defined for the cerebral cortex surface have also been studied, and serve to express spatial distributions specifically in the cortex [22]–[24].

Studies dealing with the *structural aspect* of the cerebral cortex can consist of collecting observations and retrieving from this collection statistics for the most likely structural occurrence of the sulci and their connections [4]. When applied to *in vivo* observations through MRI, skeletonization methods have been used to represent explicitly the cortical topography (see also [5] for more complete discussion). For example, in [25] brain segmentation is performed using a contour detection followed by a morphological closing in order to fill the sulci. The set of points belonging to the sulci are defined by the difference between the closed brain and the segmenting volume. In [22], tissue information [grey matter (GM), cerebro-spinal fluid (CSF), white matter (WM)] are computed using an automatic threshold. The outer part of the sulci are represented by a set of curves obtained from the skeletonization of the CSF located on the superficial traces of the cortical sulci. These methods only capture the superficial component of the sulcal topography while two thirds of the total cerebral cortex surface is buried within the cortical folds. Concerning the segmentation of the buried part of the cortical sulci, Szekely *et al.* [26] proposed a 3-D extension of the medial axis transform applied to the binary complement of the brain. A 3-D skeletonization method robust to common topological artifacts has also been introduced in [27]. In these last two methods the final representation of the cortical topography is a set of volumetric surfaces representing the buried part of the cerebral sulci. The main disadvantage of methods based on skeletonization resides in their weakness in representing the cortical folds in a form adapted for visualization or for morphometric computation purposes. For the latter, a parametrical representation of the cortical sulci, which defines a natural coordinate system for these entities, is much more suitable. In particular, length, depth, or higher shape parameters can be directly computed from this kind of representation [28]. Moreover, an analytical

description of cortical sulci, associated with a 3-D geometric rendering algorithm, reveals the complex shapes of sulci [29].

The method we have developed to represent the cortical topography is based on an initial skeletonization to retrieve the cortical structural component. As a result we obtain at this step a set of curves representing the exterior trace of each sulcus. We apply our active ribbon method to each of these curves in order to generate a parametric surface for each cortical fold [5]. A very similar approach has been developed simultaneously with ours in [30]. However, this last approach differs from ours by the fact that in this application only an active contour is used to model the median surface of a sulcus, while our active ribbon method use a two-step strategy evolving from an active curve to an active surface. The set of forces that are used to fit the active model to the median surface of a sulcus differs also in these two applications.

When dealing with the sulcus recognition task, we propose a first step toward this problem by the use of sulcus spatial priors. We do not focus on a fully automatic recognition algorithm (see for that [22], [25], [31]) as a common standard nomenclature for sulcal topography is not fully defined yet. In our opinion, the problem resides more in the definition of a way to present objective information to help the user (anatomist, neurosurgeon, etc.,) in the labeling task than in a fully automatic process which will be valid only for the main sulci.

III. Modeling of the Cortical Topography

Cerebral cortex cartography is based on its subdivision in a set of sulci and gyri. 3-D MRI images distinguish between the different cerebral tissues (GM, WM) and CSF, providing an *implicit* representation of the cortical folds. A structural representation of the cortical landmarks requires an *explicit* representation of these elements and their organization. The method we have developed to extract, from 3-D MRI, the cortical topography is divided into two steps.

1) Extraction of the exterior trace of the sulci and detection of the connections between these entities. At this level, we extract the superficial structural topography of the cortical topography.
2) Modeling of the deeper cortical infolding by tracking the median surface of each cortical fold. As a result, we obtain a set of parametric surfaces representing the 3-D shape of the buried part of each sulcus.

Finally, a set of parameters are associated with each extracted fold and junction. The main steps of this procedure are described below.

A. Extraction of Exterior Sulcal Pattern

The method is based on the following procedure:

1) Input Data: For this study, input data were 3-D MRI acquired on a Philips Gyroscan ACS 1.5 Tesla superconducting magnet system. The following sequence was used: T1-weighted 3-D spoiled gradient-echo acquisition with sagittal volume excitation (TR = 18, TE = 10, flip angle = 30°, 140–180 sagittal slices).

The following processes are applied to these data. Since the first four steps (refer to Fig. 1) have been described in detail elsewhere, we summarize them only briefly here, and make reference to the original work.

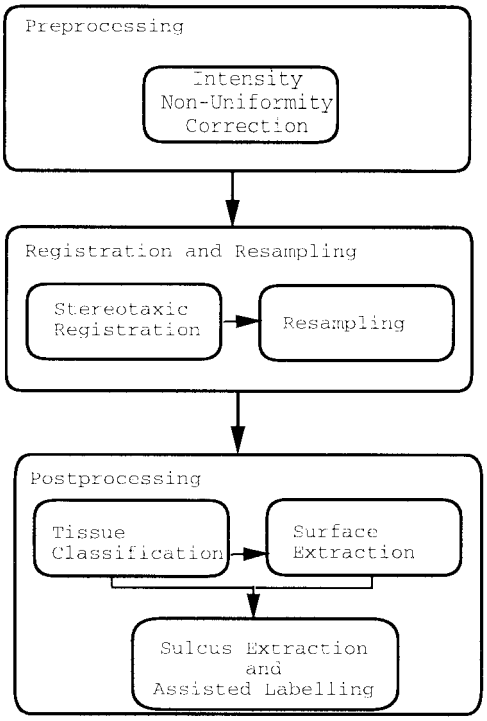

Fig. 1. Pipeline flowgraph. This figure represents the pipeline processing applied to each 3-D MRI data set before sulcal extraction as realized with SEAL.

Step 1—Correction for 3-D Intensity Nonuniformity: A major problem for automated MRI image segmentation is the slowly varying change in signal intensity over the image, caused principally by nonuniformities in the radiofrequency field. Apparent signal from one tissue type is therefore different from one brain area to another, confusing automated classification algorithms that assume constant signal for one tissue type. Such artifacts are removed by a fully automated 3-D technique for inhomogeneity correction developed in our lab [32].

Step 2—Automated 3-D Stereotaxic Transformation: In order to account for interindividual differences in absolute brain size, each brain was separately transformed into a standardized (i.e., Talairach-like) stereotaxic space and resampled on a 1 mm^3 voxel grid. This was done using an automatic registration program which uses a 3-D cross-correlation approach to match the single MRI volume with the intensity average of 305 MRI brain volumes previously aligned in standardized stereotaxic space [33]. The method requires no manual identification of points or contours and therefore does not suffer from drawbacks associated with user intervention such as reproducibility and interobserver variability.

Step 3—Tissue Classification: An artificial neural network classifier was applied to identify grey/white/CSF tissue types [34]. This method uses spatial priors on the location of each tissue type (this last condition implies that all computations must be carried out in common referential frame, as realized in Step 2).

Step 4—Cerebral Cortex Surface Extraction: A geometric surface representing the interface between the cerebral cortex

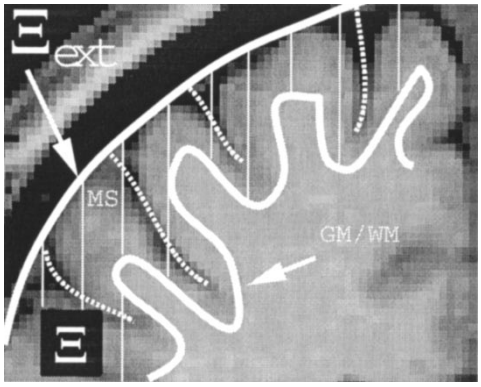

Fig. 2. Region of interest Ξ. This image shows a 2-D section of Ξ [the region bordered by the bounding hull of the brain ($\Xi_{\rm ext}$) and the grey matter/white matter interface (GM/WM)] $\Xi_{\rm ext}$ is obtained when a morphological closing (dilatation followed by an erosion) is applied to $(\Omega(\text{GM}) + \Omega(\text{WM}))$. In the region Ξ we are looking for voxels which belong to the sulcus median surface (MS) (dashed lines).

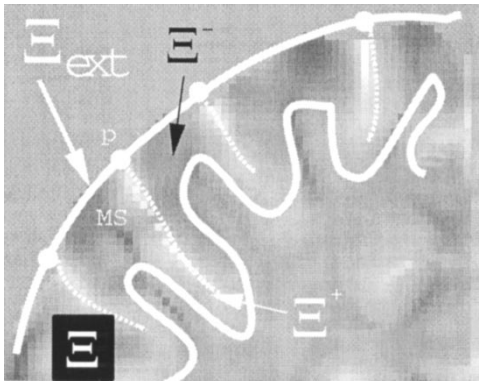

Fig. 3. Curvature analysis and detection of the exterior traces of the sulci. For each voxel which belong to Ξ we can compute its mean curvature (or ML_{vv}). The sign of the mean curvature is positive for voxels which are in the sulci (bright area, noted Ξ^+) and negative for voxels located in the gyri ridges (dark area, noted Ξ^-). P is a voxel located on the convex bounding hull of the brain, it has a positive ML_{vv} value. P is a voxel belonging to the $\Omega_{\rm TopoExt}$ set.

GM and the extracerebral CSF is automatically extracted using an iterative minimization of a cost function [35]. This last step separates voxels belonging to the brain from those located in the cerebellum.

These first four image processing steps have been already published in the literature and have been validated in the context of automatic multiple sclerosis quantification in a large multicenter clinical trial context [34]. In our application, these preprocessing stages allow us to extract two sets of voxels corresponding, respectively, to the grey and white matter. The processing described below does not depend on these particular algorithms. In fact, any procedure that results in a set of classified cerebral voxels of grey and white matter can be used to preprocess the data.

The following steps address the task of sulcal segmentation more specifically:

Step 5—Definition of the Cortical Region of Interest: We define a region of interest (ROI), noted Ξ, representing the set of voxels which belong to the GM and the CSF included in the cortical folds (sulcal CSF)

$$\Xi = \{(\Omega(GM) + \Omega(WM)) \bullet C_{\rm struct}\} \setminus \Omega(WM) \quad (1)$$

where

$\Omega(GM)$	GM set;
$\Omega(WM)$	WM set;
$+$	addition between sets;
$\setminus$	difference between sets;
$\bullet$	morphological closing [36];
$C_{\rm struct}$	spherical element of radius 5 mm.

The goal of the morphological closing is to fill the interspace between adjacent walls of a sulcus. When completed voxels which belong to the sulcus median surface will be part of this ROI (refer to Fig. 2).

Step 6—Curvature Analysis: Voxels which belong to Ξ can be divided in two main anatomical components: sulci and gyri. An anatomical decomposition of Ξ into convex and concave sets using differential geometry identifies gyral and sulcal voxels. We have previously presented such an approach in [37]. We know that for each voxel ν which belongs to Ξ, there is an iso-surface passing through it. This surface can be described, in the neighborhood of the voxel ν, by the two principal curvatures (k_1 and k_2) and their combinations: mean curvature $[m = (k_1 + k_2)/2]$ and Gaussian curvature $[g = (k_1 * k_2)/2]$. We use the sign of the mean curvature (or more exactly the sign of the mean L_{vv}, noted ML_{vv}, an operator highly related to the mean curvature introduced in [38]) to distinguish two sets of voxels

$$\Xi = \{\Xi^+, \Xi^-\} \quad (2)$$

where Ξ^+ and Ξ^-, the set of voxels having positive and negative ML_{vv} values which represent sulci and gyri, respectively (refer to Fig. 3).

Step 7—Detection of the Exterior Traces of the Sulci: Voxels which belong to the superficial trace of the sulci are defined by

$$\Omega_{\rm TopoExt} = \{\nu \setminus \nu \in (\Xi_{\rm ext} \cap \Xi^+)\} \quad (3)$$

Fig. 4. Detection of the exterior traces of the sulci. A 3-D rendering of the superficial traces of cortical sulci superimposed on the cerebral cortex surface (refer to Step 8 in Section III-A). Junctions between these curves are also detected. These two elements (curves, junctions) represent the structural organization of the superficial cortical topography.

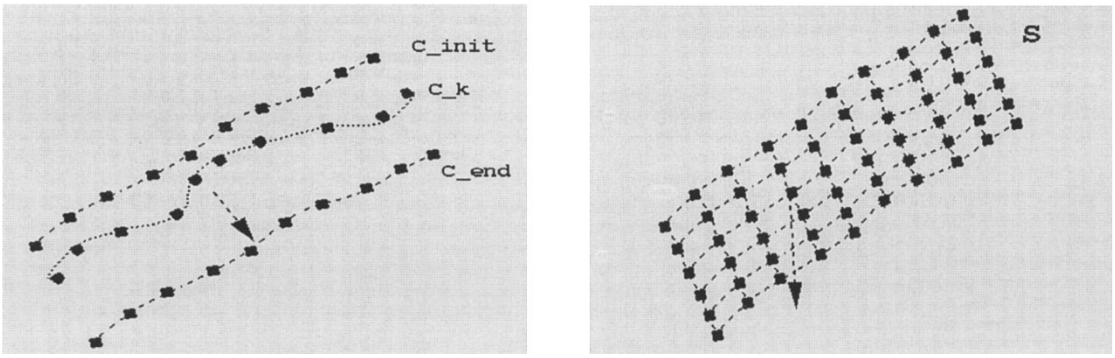

(a) (b)

Fig. 5. Active ribbon method. (a) First step of the active ribbon method: a curve initialized on the superior trace of a sulcus (C_init) is submitted to a set of forces and converge toward the sulcal fundus (C_end). (b) Successive loci of the active curve are resampled and serve to construct an active surface (S) that will model the sulcus median surface.

with Ξ_{ext} the bounding hull of the cerebral cortex. More explicitly, Ω_{TopoExt} is the set of voxels, located on the bounding hull of the brain, having a positive ML_{vv} value (refer to Fig. 3 and see the example of point P).

Step 8—Thinning: We then apply a thinning method [39] to the Ω_{TopoExt} set in order to extract a set of thin curves and junctions representing the superficial parts of the cerebral sulci.

We obtain a structural decomposition of the superficial cortical topography as can be seen on Fig. 4. This structural decomposition can be encoded in a graph structure $G = (C, A)$ where C is a set of curves and A is a set of junctions.

Discussion: Concerning the sensitivity of the superficial cortical topography segmentation with regard to the preprocessing stage (Steps 1–4), one difficulty may appear during the tissue classification stage (Step 3). If the dura-matter (or vessels) have a MR intensity signal similar to the GM, due for instance to partial volume effects, then locally, it may be difficult to distinguish between these anatomical structures. This kind of artifact results in a local error of incorrect definition of the cortical ROI (Ξ) (Step 5). Since we assume in Step 6 that only two anatomical structures (sulci, gyri) are present within this ROI, any nonbrain anatomical structures may be assigned to gyri or sulci patterns. However, the use of spatial priors for the location of each tissue type [as allowed with stereotaxic registration (Step 2)], and the definition of an appropriated MR acquisition protocol [corrected for slowly-varying change in signal intensity (Step 1)] minimize such artifacts.

B. Modeling of the Cortical Sulcus Using the Active Ribbon Method

The active ribbon method is based on the active model paradigm introduced by Kass [40], and our implementation (based on the snake-spline active model described in [41]) has been previously detailed in [5].

To summarize, consider C_i, a curve belonging to the set of curves C of the graph G, representing the external trace of a sulcal fold. The active ribbon method consists of modeling this curve by a spline and subjecting it to a set of forces designed such that the active curve will move smoothly from the initial superficial trace of the sulcus (extracted in Step eight) toward the bottom of the sulcus (known as the fundus). If the successive loci of this active curve are stored, from its initial position toward its final position, a set of curves is obtained which approximately represents the median surface of the cortical fold [refer to Fig. 5(a)]. The forces that are applied to the active curve are $\{\vec{f}_1, \vec{f}_2, \vec{f}_3\}$ with

- $\vec{f}_1(x, y, zo = \vec{\nabla} POT_1(x, y, z)$*:* Where the potential $POT_1(x, y, z)$ is a distance transform computed for a volume which contains three labels [39]. These three labels are, respectively, $\{\Omega_{\text{TopoExt}}, \Xi^+, (\Xi^+)^{\text{comp}}\}$ where $()^{\text{comp}}$ is the binary complement of the associated set. POT_1 gives for each voxel which belongs to Ξ^+ the length to the closest voxel of Ω_{TopoExt}, for a path composed of voxels which belong to Ξ^+. This length is maximum between a voxel which belongs to the superficial trace of a sulcus and a voxel located on the fundus. This force can be considered as a penetration force which drives the active curve from its initial superficial trace toward the fundus (refer to Fig. 6).
- $\vec{f}_2(x, y, z) = -\vec{\nabla} POT_2(x, y, z)$*:* Where the potential $POT_2(x, y, z)$ is a distance transform [42] computed on the binary volume $(\Xi^-, (\Xi^-)^{\text{comp}})$. This second potential represents the distance between a voxel which belongs to Ξ^- and the closest voxel which has a positive ML_{vv} value. This potential is nulled when each point of the active curve is inside the sulcus. This second potential is used to prevent the active curve from moving outside a sulcus (refer to Fig. 7).
- $\vec{f}_3(x, y, z) = \vec{\nabla} POT_3(x, y, z)$*:* The potential POT_3 (x, y, z) is defined as being the ML_{vv} intensity map. This potential is maximized when the active surface exactly fits the median surface of a sulcus, and corresponds to the location of the maximum of the ML_{vv} operator (bright area on Fig. 3).

The second step of the active ribbon method consists of modeling this first approximation of the fold's median surface by an active surface submitted to a second set of forces in order to make it converge toward the actual median surface of the fold [refer to Fig. 5(b)]. This second step improves the quality of the segmentation by using an active model having the same codimension (the same number of parametrical indices) as the underlying anatomical structure we want to extract (the median

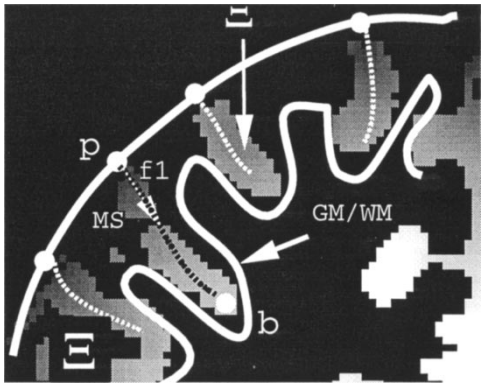

Fig. 6. First potential. The first force $\vec{f}_1$ applied to the active curve is $\vec{f}_1(x, y, z) = \vec{\nabla} POT_1(x, y, z)$. This image represents a section of potential POT_1. This potential gives the length of the path between b and p when the path is composed of voxels which belong to Ξ^+ (bright voxels). This potential estimates the sulcus depth (even if the shape of the sulcus is convoluted), then $\vec{f}_1$ can be seen as a force of penetration which allows the active curve to move toward the sulcal fundus.

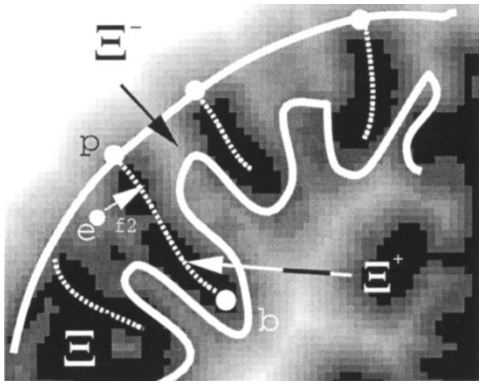

Fig. 7. Second potential. When the active curve moves from p to b some points of the curve can be outside a sulcus (point e on this figure is outside Ξ^+). Also, we design $\vec{f}_2(x, y, z) = -\vec{\nabla} POT_2(x, y, z)$, a force that allows to prevent the active curve from moving outside a sulcus.

surface of the sulcus). The forces that are applied to the active surface are $\{\vec{f}_4$ and $\vec{f}_5\}$ where the following pertains.

- $\vec{f}_4(x, y, z) = \vec{f}_3(x, y, z)$.
- $\vec{f}_5(x, y, z) = -\vec{\nabla} I(x, y, z)$: where $I(x, y, z)$ is the intensity map of the 3-D MRI volume. The median surface of a sulcus is filled with CSF and has a low grey level value on T1-weighted MRI data. This potential is minimized when the active surface best fits the sulcus median surface (by maximally overlapping the sulcal CSF).

The active ribbon method allows for the retrieval of a parametric surface representing the median surface of each fold of the cerebral cortex. Parametric representations of cortical sulci obtained with this method are shown in Figs. 8 and 14.

Discussion: During the first step of the active ribbon method, a set of three forces ($\{\vec{f}_1, \vec{f}_2, \vec{f}_3\}$) is defined to drive the model from the sulcus superficial trace, to its fundus. During the second stage two forces ($\{\vec{f}_4, \vec{f}_5\}$) refine the active ribbon to fit the sulcus' median surface. Weighting factors are applied to each of these forces in order to insure correct behavior of the active ribbon. Finding the value for each of these weighting factors can be posed as an optimization problem (find the optimum weighting factor values that allow to minimize the objective function). This kind of approach has been studied in the literature, but from our knowledge no general solution has been found yet. In our application these weighting parameters were considered as heuristics and were experimentally defined. We found that $w1 = +1.5$, $w2 = -1.0$, and $w3 = +1.0$ were the best heuristic values. The sign allows to maximize or minimize the associated potential. Taking the first weighting factor with a value superior to 1.0 gives more importance to the *penetration force* and allows the active model to reach the sulcal fundus even with complex shape configurations (like those occurring where there exists a high variation of the orientation of a sulcus).

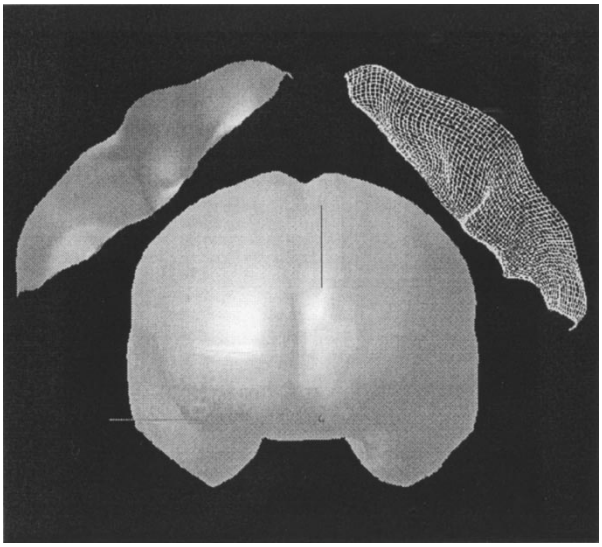

Fig. 8. Numerical modeling of cortical sulci using active ribbons. Front view showing the parametrical representation of the left and right central sulcus as retrieved with the active ribbon method (note that the brain model, displayed at 50% of its original size, is only used to figure the orientation).

C. Graph Encoding—Representation of the Cortical Topography

The representation of the cortical sulcal topography is directly derived from these results. The graph G defined in Section III-A becomes

$$G_{CSST} = \{F, J\} \tag{4}$$

where G_{CSST}, the graph representing the cortical sulcal schematic topography of a particular subject, is composed of F a set of f folds and J a set of j junctions.

- F_i, $i \in \{0, f-1\}$ stores the information associated with each fold, namely:
  - — the parametric surface of the cortical fold;
  - — the set of morphometrical parameters (length, depth, orientation);
  - — the set of labels (*hemisphere*, *lobe*, *sulcus_name*, *sulcus_type*[1]) where *sulcus_name* has value in the set

[1] Primary, secondary, and tertiary.

$\Theta = \{$unknown, frontal_superior, frontal_median, frontal_inferior, central, ..., side_branch$\}$. A labeling of the graph is performed when each *sulcus_name* attribute of each fold (F_i, $i \in \{0, f-1\}$) is associated with a specific label θ of the set Θ.

- J_i, $i \in \{0, j-1\}$ is a junction, and stores:
  - — its 3-D location;
  - — the list of folds which connect at this node.

IV. Validation and Statistical Analysis of Cortical Topography

The labeling of the 3-D shape of a sulcus is time-consuming and subject to significant inter- and intra-rater variability, especially when dealing with complex 3-D folds. In contrast, our modeling method allows the user to obtain a 3-D representation of a cortical sulcus with minimum human intervention (the user is asked only to select a set of automatically extracted surfaces corresponding to the sulcus of interest). In this section we present experiments showing: 1) that our sulcal extraction method is reliable and is comparable to results obtained manually and 2) that the cortical topography modeling performed allows for the retrieval, from a set of labeled graphs, of statistical information about both spatial and structural component of the cortical topography.

A. Extraction of Morphometrical Statistics

1) Validation of the Active Ribbon Method: In order to evaluate the active ribbon method, we compare manual *versus* semiautomatic delineation for a set of four main sulci extracted on 20 MRI datasets. The voxels of the 3-D median surface of the central sulcus and the superior frontal sulcus of both hemispheres were manually labeled by an anatomist using an interactive 3-D visualization program [43]. This program allows for the simultaneous visualization of 3-D movement through the sagittal, axial, and coronal planes of high resolution MRI as well along a reconstructed 3-D surface rendering of the brain. The same sulci were extracted with the active ribbon method.

In order to compare the active-ribbon *versus* the manual labeling, we first used a distance transform method to measure the root mean square (rms) distance between the two digital representations. The rms is computed as follows:

$$\mathrm{rms}_{\mathrm{am}}^2 = \frac{1}{\mathrm{card}(\Omega_{\mathrm{auto}})} \sum_{\nu \in \Omega_{\mathrm{auto}}} (d^{\mathrm{am}}(\nu))^2 \quad (5)$$

$$\mathrm{rms}_{\mathrm{ma}}^2 = \frac{1}{\mathrm{card}(\Omega_{\mathrm{manual}})} \sum_{\nu \in \Omega_{\mathrm{manual}}} (d^{\mathrm{ma}}(\nu))^2 \quad (6)$$

with $\mathrm{card}(\Omega_{\mathrm{manual}})$: the number of voxel manually labeled; $\mathrm{card}(\Omega_{\mathrm{auto}})$: the associated set of voxels labeled with the active ribbon method.

Distance measures (d^{am} and d^{ma}) are calculated by computing a distance transform [42] between each point of the parametrized surface and the manually traced sulcus. This distance transform gives for each point of the parametrized surface the distance to its closest point in the manually traced sulcus. We note d^{am} the distance between the automatic and the manual labeling. High values indicate a significant difference between the automatic and manual labeling. However, this distance does not reflect the accuracy of the active model in covering a sulcus in its full extent. Therefore, we measure the error d^{ma} (where ma stands for manual *versus* automatic) which represents the distance between the manual and the automatic labeling. This second error will be high when there is a significant difference between the manual and the automatic labeling of the same sulcus. When considering a sulcus which is only partially covered with our active-ribbon method the first error d^{am} will be small, but d^{ma} will have a high value.

TABLE I
RMS Distance Between Manual and Semiautomatic Labeling. SCL: Central Sulcus of Left Hemisphere; SCR: Central Sulcus Right; FrontSupL: Superior Frontal Sulcus Left; FrontSupR: Superior Frontal Sulcus Right; Distances are Given in Millimeters

	auto vs. manual		manual vs. auto	
	mean rms	max rms	mean rms	max rms
SCL	1.16	3.32	0.91	2.51
SCR	1.41	2.65	1.70	2.66
FrontSupL	0.95	1.55	1.54	3.91
FontSupR	0.89	2.18	1.34	3.99

The rms measure gives information about the mean errors between the two labeling for this set of 20 experiments. As can be seen on Table I, the mean rms between manual *versus* active-ribbon labeling has a value of 1.10 mm. The mean value of rms when active-ribbon labeling was taken as the standard is 1.37 mm. A symmetric error estimate is given by the mean value of this two measures and has a value of 1.24 mm. This means that the average error between two labeling is less than two voxels for a 1 mm^3 isotropic MRI volume. These results shows that the 3-D structure of the cortical sulci as retrieved by the active ribbon modeling is similar to the result obtained by manual labeling.

We have also computed the maximum distance between the manually labeled sulcus and its associated automatically extracted representation to evaluate the accuracy of our sulcal segmentation method. We obtained, for each of the four sulci, a maximum distance between the two labeling for each of the 20 subjects. We note $d_{\max}^{\mathrm{am}}$ the maximum distance found between the automatic and the manual labeling and $d_{\max}^{\mathrm{ma}}$ the maximum distance between the manual and the automatic labeling. Since a distance transform is used to estimate these errors, the automatically extracted parametrical surface must be voxelized. As we compare the binary volume resulting from the voxelization of a parametrized surface with its associated manually labeled binary volume the minimum nonzero value for $d_{\max}^{\mathrm{am}}$ or $d_{\max}^{\mathrm{ma}}$ will be 1 mm for a 1 mm^3 isotropic MRI volume.

In order to evaluate the mean error between two labeling, we have also computed the mean error distance. The mean error distance is computed by averaging the sum of all the distances between two corresponding labeling. We then obtain, as previously, two measures: $\overline{d}_{\mathrm{mean}}^{\mathrm{am}}$ and $\overline{d}_{\mathrm{mean}}^{\mathrm{ma}}$ representing, respectively, the mean distance error between the automatic *versus* the manual labeling and the mean distance error between the manual *versus* the automatic labeling. We measure

TABLE II
GLOBAL MAXIMUM OF ERROR MEASUREMENTS (20 SUBJECTS). SCL: CENTRAL SULCUS OF LEFT HEMISPHERE; SCR: CENTRAL SULCUS RIGHT; FRONTSUPL: SUPERIOR FRONTAL SULCUS LEFT; FRONTSUPR: SUPERIOR FRONTAL SULCUS RIGHT; DISTANCES ARE GIVEN IN MILLIMETERS

	auto vs. manual			manual vs. auto		
	d^{am}_{max}	d^{am}_{mean}	σ	d^{ma}_{max}	d^{ma}_{mean}	σ
SCL	4.98	1.27	0.19	1.98	1.27	0.82
SCR	3.98	1.24	0.55	1.98	1.12	1.10
FrontSupL	3.98	1.32	1.07	3.98	1.54	1.11
FontSupR	3.98	1.40	1.06	2.98	1.35	0.81

also their associated standard deviation σ. The closer to zero these measures are, the most likely the difference between the two labeling will be restricted to at most one voxel.

Results can be seen in Table II. This table shows only the maximum of each measure for the 20 subjects. Therefore this table represent the worst case. The global maximum distance is obtained for the segmentation of the left central sulcus and has a value of 4 mm. This kind of high distance error can occur in a specific case: when the superior part of the central sulcus has a strong connection with the interhemispheric plane. In this case there is nothing in our low-level algorithm to prevent one part of the active model from falling into the interhemispheric plane. This error was found on a single subject. The correction of this kind of error, due to strong connection between adjacent sulci, implies the use of higher level model containing more *a priori* knowledge on the shape of each sulcus to prevent the active model from taking unlikely configurations. We have also noticed that the inferior ending of the central sulcus is sometimes difficult to localize with accuracy due to a connection with a tertiary sulcus (subcentral sulcus). In this case, the ending of the central sulcus is not well defined, leading to possible differences between the manual and the automatic labeling.

The main differences between the manual and the automatic labeling occurs at the ends of the sulci. This is illustrated on Fig. 9. On this image we have superimposed lines representing the manually labeled superior trace and sulcal fundus (dashed curves) and the median surface as retrieved with the active ribbon method. One can see that the active ribbon failed to detect the exact location of the sulcus ends as determined by the expert. However the difference is very small, i.e., inferior to 5 mm. The reason for this difference is generally the low value of the sulcus depth at these location. On the other hand, for the same reason (i.e., low depth), tertiary sulci (i.e., highly variable superficial sulci) and vessels imprints are not detected, improving robustness of sulcal topography detection with respect to these small artifacts.

2) Computation of Morphometric Parameters: The parametric representation of the 3-D shape of a sulcus as retrieved by the active ribbon method can be directly used to compute morphometrics such as length and depth. We have measured these parameters for the central sulcus extracted from 20 MRI datasets. The results are shown in Table III and compared to the results obtained by Ono for similar sulci from 25 autopsy specimen brains [4].

Measurement obtained through our method are very similar to those given by Ono.

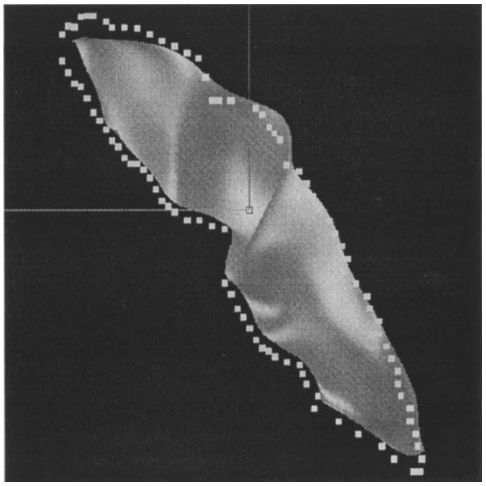

Fig. 9. Comparison of manual and automatic labeling. Front view showing the parametrical representation of the left central sulcus as retrieved with the active ribbon method. The two dashed lines represent, respectively, the manual labeling of the sulcus superficial trace and the sulcus fundus. One can see that there is a small difference between automatic and manual labeling at sulcus ends. The reason for this difference is generally the low value of the sulcus depth at these locations which makes their automatic detections very difficult. However, differences between manual and semiautomatic labeling at these locations remains with a value inferior to 5 mm.

TABLE III
MORPHOMETRICS FOR THE LEFT AND THE RIGHT CENTRAL SULCUS COMPUTED FROM 20 SUBJECTS. THE MINIMUM AND MAXIMUM VALUE FOR EACH MEASURE ARE SHOWN BETWEEN BRACKETS. FOR EXAMPLE THE MIMIMUM VALUE FOR THE LENGTH OF THE LEFT CENTRAL SULCUS FOUND BY ONO HAS A VALUE OF 70 MM WHILE THE MAXIMUM LENGTH IS 125 MM

	Left		Right	
	Length (mm)	Depth (mm)	Length (mm)	Depth (mm)
ONO	94(70-125)	16.0(7-22)	105(88-127)	16.6(6-30)
SEAL	103.8(86-126)	17.2(15-22)	104.7(93-121)	17.7(12-21)

Moreover, on 20 MR scans the fundus of the central sulcus was manually labeled using an interactive display software [43]. The length of the central sulcus bottom line was then computed from this set of manual labeling. When compared to measures obtained semiautomatically with the active ribbon method, we found a mean difference of 5 mm between the two sets of measurements. In most cases the lengths obtained from the automatic labeling have a value 5 mm less than the associated manual labeling. This is due to the difficulty in detecting the exact location of the sulci starts and ends due to the low depths of these boundaries.

B. Validation of the Structural Information

Before collecting information about the structural occurrence of the cortical sulci, it is essential to study the stability of the retrieved global structural component of the cortical topography with respect to noise and shading effects common on MR scanning. Experiments were realized using an MRI simulator. Magnetic resonance images are simulated by MRISIM [44], a program that predicts image contrast by computing MR signal intensities from a discrete-event simulation of pulse sequences based on the Bloch equations. In order to simulate realistic MRI images of the human brain using MRISIM, a realistic high-resolution brain phantom was

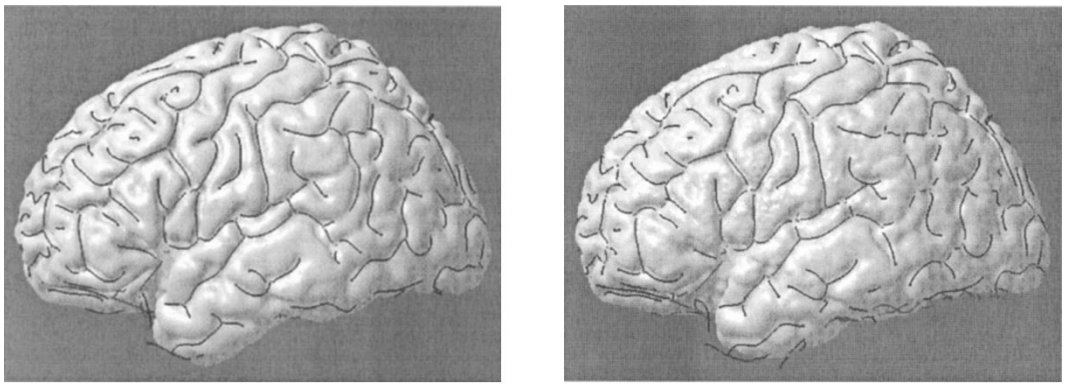

(a) (b)

Fig. 10. Sensitivity to noise and RFI. (a) Structural decomposition of the cerebral topography retrieved from an MRI with 0% noise and 0% radio-frequency inhomogeneities. (b) Same computation for the MRI with 9% noise and 20% radio-frequency inhomogeneities; note also the difference in cortical surface due to these artifacts.

TABLE IV
STRUCTURAL DECOMPOSITION OF THE CORTICAL TOPOGRAPHY OF THE SAME BRAIN FOR DIFFERENT LEVELS OF MRI DEGRADATIONS (NOISE AND RFI)

	gold	noise 1%	noise 3%	noise 9%	noise 9% RFI 20%
number of vertices (left hemisphere)	238	252	246	255	264
number of vertices (right hemisphere)	247	266	270	249	296
Total Vertices	485	518	516	504	560
number of junctions (left hemisphere)	210	215	210	223	228
number of junctions (right hemisphere)	203	205	216	208	217
Total Junctions	413	420	426	431	445

used to map tissue intensities into MR images [45]. The simulator accounts for the effects of various image acquisition parameters by incorporating partial volume averaging, noise and radio frequency inhomogeneity (RFI). The phantom serves as a gold standard to measure the performance of different image processing algorithms. It has been used previously in validation studies for correction of intensity inhomogeneity (Step 2, Section III-A) and tissue classification (Step 3, Section III-A). In our application, we want to study the sensitivity of our method with respect to noise and RFI in the detection of the superior traces of the sulci. We present, in the following table (Table IV) the structural decomposition of the same brain imaged with different noise and RFI levels.

Table IV shows that a variation of 15% on the number of vertices and 8% on the number of junctions can be found for the same subject, depending on noise and RFI effects. These variations are for a part due to *intrinsic* sensitivity of our sulcal superficial topography detection method but also due to the sensitivity all the preprocessing steps involved in the method (e.g., tissue classification and cerebral cortex surface extraction). In Fig. 10 we compare the retrieved cerebral topography computed with, respectively, a 0% noise and 0% RFI effect, and a 9% noise, 20% RFI effect. Visual comparison of these two segmentations shows that a stable structural decomposition of the brain cortical topography was retrieved for the main cortical landmarks with SEAL within the standard range of noise and shading artifacts.

TABLE V
RMS DISTANCES BETWEEN SIMILAR PARAMETRIZED SURFACES EXTRACTED WITH DIFFERENT LEVELS OF MRI DEGRADATION (NOISE AND RFI). SCL: CENTRAL SULCUS OF LEFT HEMISPHERE; SCR: CENTRAL SULCUS RIGHT

	(noise 0% RFI 0%) vs. (noise 9% RFI 20%)	(noise 9% RFI 20%) vs. (noise 0% RFI 0%)
SCL	0.69	0.46
SCR	0.74	0.51

We can also evaluate the behavior of the active ribbon method with respect to noise and RFI artifacts from these simulated data. The median surface of central sulcus was extracted from the 0% noise, 0% RFI MRI and from the 9% noise, 20% RFI MRI. We computed the rms distance between the two obtained parametrized surfaces. Results are shown in Table V. A maximum rms of 0.7 mm was found between two similar parametrized surfaces, showing that our method (including all preprocessing steps) is very robust to common noise and RFI effects.

C. Generation of Sulcal Probability Maps

As stated in the introduction, neuroanatomical spatial variability can be quantified in the form of 3-D stereotaxic maps where each voxel expresses the likelihood of finding a particular structure at that location. By averaging the labelling of structures in an ensemble of stereotaxic MRI volumes, a continuous 3-D probability field (0.0–1.0 at each voxel) for that structure, termed a statistical probability anatomy map (SP_AM), can be constructed [46]. In order to study the accuracy of our shape modeling method for generating these structures, we compare SP_AM's generated by manual labeling and by semiautomatic labeling, as performed with the active ribbon method (see Fig. 11). 3-D maps of the central sulcus and superior frontal sulcus for both hemispheres were compared. At each voxel, the manual and semiautomatic SP_AM's were compared by substracting their respective values

$$\Delta(x_i, y_i, z_i) = \left|\mathrm{SP\_AM}_{\mathrm{manual}}(x_i, y_i, z_i) - \mathrm{SP\_AM}_{\mathrm{semi\_automatic}}(x_i, y_i, z_i)\right| \quad (7)$$

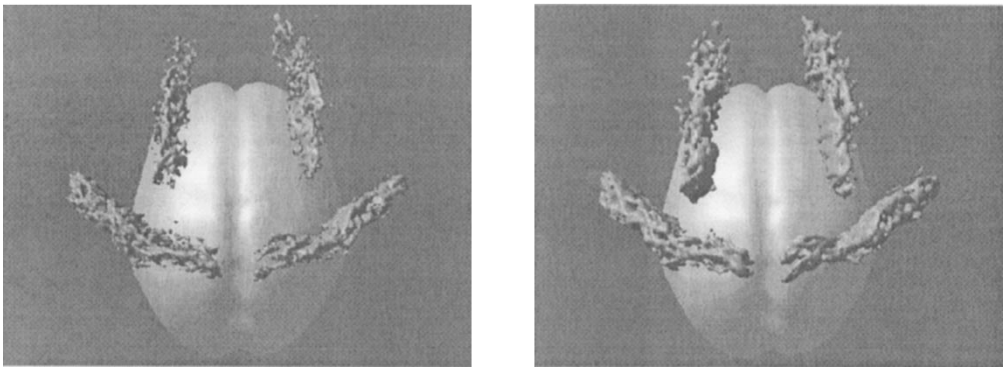

(a) (b)

Fig. 11. Manual versus semiautomatic SP_AM's. (a) 3-D iso-surface of the central and superior frontal sulcus SP_AM's obtained by manual labeling of a set of 21 subjects. (b) Equivalent 3-D SP_AM's computed from the associated 21 labeled graphs (displayed reduced model brain is used to figure the general orientation).

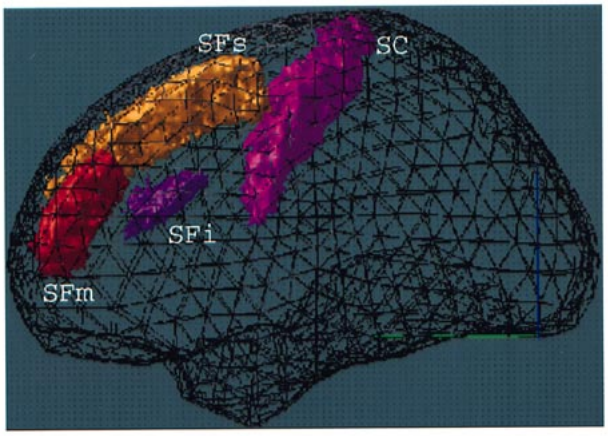

Fig. 12. Probability maps. Example of sulcus probability maps (SP_AM's) computed in stereotaxic space from 36 subjects. SC: central sulcus, SF's: superior frontal sulcus, SFm: middle frontal sulcus, and SFi: anterior part of the inferior frontal sulcus.

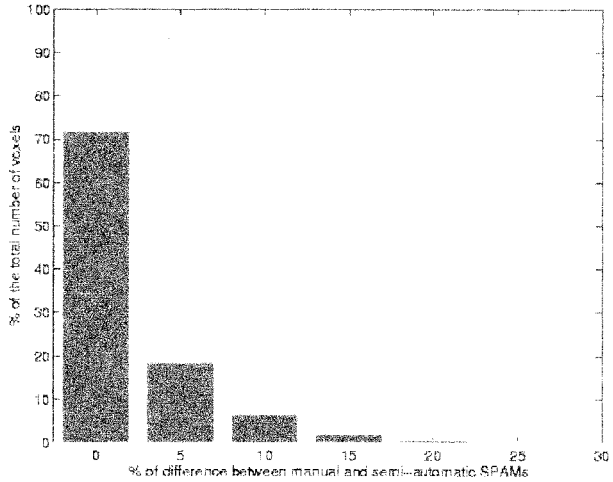

Fig. 13. Percentage of difference between manual and semiautomatic SPAM's. This figure shows the fraction (in percentage) of the total number of voxels that differ between the manual and the semiautomatic SP_AM. Since only 3% of the SP_AM voxels differ in value by more than 10%, we conclude that the semiautomatic SP_AM is similar to the manual SP_AM.

where $\text{SP\_AM}_{\text{manual}}(x_i, y_i, z_i)$ and $\text{SP\_AM}_{\text{semi\_automatic}}$ (x_i, y_i, z_i) store the probability of finding a given sulcus at the 3-D location (x_i, y_i, z_i). A histogram of differences found between these two SP_AM's is displayed in Fig. 13. Only nonzero voxels form the manually created SP_AM are compared to the automatically generated SP_AM. Since we are working with probability values, the maximum error value at a 3-D location could be 1.0. The histogram demonstrates that 90% of the total number of voxels differ by 5% or less between the two SP_AM's. This value corresponds to a difference between the manual and the semiautomatic labeling to a maximum of one case out of 20 at the same 3-D location. The difference between manual and semiautomatic SP_AM's remains inferior to 0.15 (15% of difference or a maximum of three errors upon 20 in the labellings at the same 3-D location) for 97% of the total number of voxels. Therefore, we conclude that SP_AM's computed from a set of labeled graphs yields results similar to those generated by manual labeling. It is important to note here that the observed differences are not necessarily due to an error in the semiautomatic labeling but could also be due to errors in the manual labeling of these complex 3-D patterns. In future work, it would be particularly interesting to compare these results with measures of inter-rater variability. However, since the labeling of the sulcal median surface is time consuming (30 min per brain), an inter-rater variability study is beyond the scope of this paper.

V. Automatic Labeling Using Sulcal Probability Maps

In this section, we describe how SEAL-derived statistical maps of sulcal distribution can be used to assist the cerebral cortex labeling. A probabilistic atlas of sulcal spatial distributions can be useful to decrease the configuration space of the recognition problem by considering only a limited set of labels acceptable for each vertex of the graph. We consider, when labeling a specific vertex, only labels that correspond to structures that are located within the corresponding area of stereotaxic space.

The sulcal neuroanatomy of 36 right-handed adults (17 female and 19 male), with no previous history of neurological or psychiatric disorders, were labeled by an experienced neu-

(a) (b)

Fig. 14. (a) Manual labeling performed by an anatomist. (b) Automatic labeling using sulcus spatial priors. Using information about sulcus spatial priors an automatic labeling of the cortical sulci can be performed. Here a color is associated with each sulcus name. Associated information for the selected curve (see the cursor) are, for example, length = 75.7 mm; depth = 15.9 mm; sulcus name probability given SP_AM: central sulcus: $p = 0.300$, postcentral sulcus: $p = 0.033$, precentral sulcus: $p = 0.014$, intraparietal sulcus: $p = 0.003$. Its "true" name being central sulcus. This illustrates one application of a 3-D numerical atlas of cortical sulci.

roanatomist [47]. Subjects' mean age was 26.0 yr (SD = 5.3). There was no sex difference in these subjects' age at the time of scanning. In order to account for interindividual differences in absolute brain size, each brain was separately transformed into stereotaxic space (refer to Step 2 in Section III-A).

A trained neuroanatomist, blinded as to hemispheric location of the sulcus by reflection of hemisphere, identified and manually labeled a restricted subset of 16 sulci: 1) the central sulcus, 2) the Sylvian fissure, 3) the superior, 4) the middle, 5) the inferior frontal sulci, 6) the ascending, and 7) the horizontal rami of the Sylvian fissure, as well as: 8) the incisura (located between these other two rami) and 9) the olfactory sulcus as well as: 10) the sulcus lateralis, 11) the sulcus medialis, 12) the sulcus intermedius, 13) the sulcus transversus (all found along the orbitofrontal surface of the brain), 14) the precentral, 15) the postcentral sulci, and finally 16) the intraparietal sulcus. These data were used to construct associated sulcal SP_AM's, representing the likelihood of finding a particular structure at each 3-D stereotaxique coordinates (refer to Fig. 12) [47].

Given these SP_AM's, we computed for each vertex the probability that its parametric representation belongs to each of the possible sulci. This information is stored within the graph structure. We can then define an initial labeling of the graph, by taking for each vertex of the graph, the sulcus' name for which the SP_AM's probability is maximum

$$\text{sulcus\_name} = \arg_{\theta \in \Theta} \max \text{prob}_{\text{SP\_AM}}(\theta) \tag{8}$$

where $\text{prob}_{\text{SP\_AM}}(\theta)$ is computed as follows:

$$\text{prob}_{\text{SP\_AM}}(S_k \in \theta) = \frac{1}{p_l * pd} \sum_{d=0}^{p_d-1} \sum_{l=0}^{p_l-1} p(S_k(u_l, v_d) \in \theta) \tag{9}$$

for a parametrical surface S_k composed of $p_l * pd$ passing points. Such an initial labeling is shown in Fig. 14(b). Due to the density of cerebral sulci and gross intersubject variability of brain shape [partially reduced through the use of the automatic linear registration (refer to Step 2 in Section III-A)], this simple use of SP_AM's is not sufficient to perform an exact automatic labeling of all the cortical sulci with total confidence [however, note the few differences between Fig. 14(a) and (b)]. In the future, we will study the use of a nonlinear registration technique (allowing to decrease remaining residual spatial miss-registration among brains that is due to normal anatomical variability [20]), associated with the use of structural *a priori* knowledge on the likelihood of sulcal pattern to improve sulcal labeling.

VI. Conclusion

We have presented an algorithm dedicated to sulcal extraction and assisted labeling, SEAL. This algorithm allows extraction of an explicit representation of the cortical folds and their arrangement on the form of a labeled graph. Statistics about both spatial and structural decomposition of the cortical topography can be retrieved from a set of labeled graphs. SEAL assists the labeling of cortical sulci by using spatial distribution priors for these structures. The program also reliably extracts standard shape parameters. Moreover, the parametric representation of the cortical sulci as retrieved with the active ribbon method can be used to compute higher order shape parameters (cf. [11], for example). We are now labeling and extracting statistics for a large number of subjects ($n = 150$). The derived statistics will be incorporated at the automatic labeling period to improve the automatic labeling.

References

[1] W. I. Welker and S. Seidenstein, "Somatic sensory representation in the cerebral cortex of the racoon (procyon lotor)," *J. Comp. Neurol.*, pp. 459–501, 1959.

[2] J. D. G. Watson, R. Myers, R. S. J. Frackowiak, J. V. Hajnal, R. P. Woods, J. C. Mazziota, S. Shipp, and S. Zeki, "Area V5 of the human brain: Evidence form a combined study using positron emission tomography and magnetic resonance imaging," *Cerebral Cortex*, vol. 3, pp. 79–94, 1993.

[3] S. Zeki, J. D. G. Watson, C. J. Lueck, K. J. Friston, C. Kennard, and R. S. J. Frackowiak, "A direct demonstration functional specialization in human visual cortex," *J. Neurosci.*, vol. 11, no. 3, pp. 641–649, 1991.

[4] M. Ono, S. Kubick, and C. D. Albernathey, *Atlas of the Cerebral Sulci.* New York: Georg Thieme Verlag, 1990.

[5] G. Le Goualher, C. Barillot, and Y. Bizais, "Modeling cortical sulci using active ribbons," *Int. J. Pattern Recognit. Artific. Intell.*, vol. 11, no. 8, pp. 1295–1315, 1997.

[6] H. Steinmetz, G. Furst, and H. J. Freund, "Variation of perisylvian and calcarine anatomic landmarks within stereotaxic proportional coordinates," *Amer. J. Neuroradiol.*, vol. 11, pp. 1123–1130, Nov./Dec. 1990.

[7] T. Paus, N. Otaky, Z. Caramanos, D. MacDonald, A. Zijdenbos, D. D'avirro, D. Gutmans, C. Holmes, F. Tomaiuolo, and A. C. Evans, "*In vivo* morphometry of the intrasulcal gray matter in the human cingulate, paracingulate, and superior-rostral sulci: Hemispheric asymetries, gender differences and probability maps," *J. Comparative Neurology*, vol. 376, pp. 664–673, 1996.

[8] O. Missir, C. Dutheil-Desclercs, J. F. Meder, A. Mussolino, and D. Fredy, "Central sulcus patterns at MRI," *J. Neuroradiol.*, vol. 16, pp. 133–144, 1989.

[9] H. Steinmetz, G. Furst, and H. J. Freund, "Cerebral cortical localization: Application and validation of the proportional grid system in MR imaging," *J. Comput. Assisted Tomogr.*, vol. 13, no. 1, pp. 10–19, Jan./Feb. 1989.

[10] J. C. Mazziota, A. W. Toga, A. C. Evans, P. Fox, and J. Lancaster, "A probabilistic atlas of the human brain: Theory and rationale for its development," *Neuroimage*, vol. 2, pp. 89–101, 1995.

[11] T. Cootes, D. H. Cooper, C. J. Taylor, and J. Graham, "Trainable method of parametric shape description," *Image Vision Comput.*, vol. 10, no. 5, pp. 289–294, June 1992.

[12] G. Subsol, N. Roberts, M. Doran, J. P. Thirion, and G. H. Whitehouse, "Automatic analysis of cerebral atrophy," *Magn. Reson. Imag.*, vol. 15, no. 8, pp. 917–27, 1997.

[13] S. Sclaroff and A. P. Pentland, "Modal matching for correspondence and recognition," *IEEE Trans. Pattern Anal. Machine Intell.*, vol. 17, pp. 545–561, June 1995.

[14] J. Talairach and P. Tournoux, *Co-Planar Stereotactic Atlas of the Human Brain: 3 Dimensional Proportional System: An Approach to Cerebral Imaging.* New York: Georg Thieme Verlag, 1988.

[15] R. Bajcsy and S. Kovacic, "Multiresolution elastic matching," *Comput. Vision, Graph. Image Processing*, vol. 46, pp. 1–21, 1989.

[16] F. L. Bookstein, "Thin-plate splines and the atlas problem for biomedical images," *Informat. Processing Med. Imag., Lecture Notes Comput. Sci.*, vol. 511, pp. 326–342, 1991.

[17] D. L. Collins, T. M. Peters, and A. C. Evans, "An automated 3D nonlinear image deformation procedure for determination of gross morphometric variability in human brain," in *Proc. Conf. Visualization Biomedical Computing*, 1994.

[18] J. C. Gee, L. Le Briquer, and C. Barillot, "Probabilistic matching of brain images," in *Information Processing in Medical Imaging (IPMI)*, Y. Bizais and C. Barillot, Eds. Ile Berder, France: Kluwer, July 1995.

[19] G. E. Christensen, R. D. Rabbitt, and M. I. Miller, "Deformable templates using large-deformation kinematics," *IEEE Trans. Med. Imag.*, vol. 5, pp. 1435–1447, Oct. 1996.

[20] D. L. Collins, G. Le Goualher, R. Venugopal, Z. Caramanos, A. C. Evans, and C. Barillot, "Cortical constraints for nonlinear cortical registration," in *Visualization in Biomedical Computing*, K. H. Höene, Ed. Hamburg, Germany, 1996, pp. 307–316.

[21] W. F. C. Barre, D. L. Collins, N. Kabani, D. MacDonald, C. Liu, M. Petrides, R. S. Kahn, and A. C. Evans, "Automated and manual identification of frontal lobe gyral cortex: A statistical probabilistic anatomical analysis," *Human Brain Mapping*, vol. 4, p. S348, 1997.

[22] N. Royackkers, H. Fawal, M. Desvignes, M. Revenu, and J. M. Travere, "Feature extraction for cortical sulci identification," in *Proc. 9th Scandinavian Conf. Image Analysis*, June 1995, vol. 2, pp. 110–121.

[23] D. MacDonald, R. Venugopal, Z. Caramanos, M. Petrides, D. Avis, and A. C. Evans, "A surface-based 2-D sulcal atlas," *Human Brain Mapping*, vol. 4, p. S414, 1997.

[24] A. Dabringhaus, T. Schormann, H. Steinmetz, G. Schlaug, K. Zilles, and P. E. Roland, "What is a standard brain? Intersubject variability of the shape of the human forebrain," *Human Brain Mapping*, 1995.

[25] S. Sandor and R. Leahy, "Surface-based labeling of cortical anatomy using a deformable atlas," *IEEE Trans. Med. Imag.*, vol. 16, pp. 41–54, Feb. 1997.

[26] G. Szekely, C. Brechuhler, O. Kubler, R. Ogniewickz, and T. Budinger, "Mapping the human cerebral cortex using 3-D medial manifolds," *SPIE Visualization Biomed. Comput.*, vol. 1808, pp. 130–144, 1992.

[27] J. F. Mangin, V. Frouin, I. Bloch, J. Regis, and J. Lopez-Krahe, "Automatic construction of an attributed relational graph representing the cortex topography using homotopic transformations," *SPIE Math. Methods Med. Imag. III*, vol. 2299, pp. 110–121, July 1994.

[28] C. Barillot, S. Champmartin, G. Le Goualher, B. Gibaud, and J. M. Scarabin, "Probabilistic modeling of brain sulci based on statistical analysis of 3D surfaces," *Human Brain Mapping*, p. S0716, 1998.

[29] C. Barillot, D. Schwartz, G. Le Goualher, B. Gibaud, and J. M. Scarabin, "3D representation of MEG/EEG data in a 3D morphological environment," *Comput. Assisted Radiol.*, pp. 249–254, 1996.

[30] M. Vaillant, C. Davatzikos, and R. N. Bryan, "Finding 3D parametric representations of deep cortical folds," in *Workshops Mathematical Methods Biomedical Image Analysis*, 1996, pp. 151–159.

[31] J. F. Mangin, J. Regis, I. Bloch, V. Frouin, Y. Samson, and J. Lopez-Krahe, "A MRF based random graph modeling the human cortical topography," in *Proc. CVRMed*, Nice, France, Apr. 1995, pp. 177–183.

[32] J. G. Sled, A. P. Zijdenbos, and A. C. Evans, "A nonparametric method for automatic correction of intensity nonuniformity in MRI data," *IEEE Trans. Med. Imag.*, vol. 17, pp. 87–97, Feb. 1998.

[33] D. L. Collins, P. Neelin, T. M. Peters, and A. C. Evans, "Automatic 3D intersubject registration of MR volumetric data in standardized Talairach space," *J. Comput. Assisted Tomogr.*, vol. 18, no. 2, pp. 192–205, Mar./Apr. 1994.

[34] A. Zijdenbos, A. C. Evans, F. Riahi, J. Sled, J. Chui, and V. Kollokian, "Automatic quantification of multiple sclerosis lesion volume using stereotaxic space," in *Proc. Visualization in Biomedical Computing (VBC), 4th Int. Conf.*, Sept. 1996, pp. 439–448.

[35] D. MacDonald, D. Avis, and A. C. Evans, "Multiple surface identification and matching in magnetic resonance images," in *Visualization in Biomedical Computing (VBC)*, Rochester, NY, 1994, vol. 2359, pp. 160–169.

[36] J. Serra, *Image Analysis and Mathematical Morphology.* London, U.K.: Academic, 1982.

[37] G. Le Goualher, C. Barillot, L. Le Briquer, and Y. Bizais, "3D detection and representation of cortical sulci," in *Proc. Computer Assisted Radiology, CAR'95*, 1995.

[38] J. B. Antoine Maintz, Petra A. van den Elsen, and M. A. Viergever, "Evaluation of ridge seeking operators from multimodality medical image matching," *IEEE Trans. Pattern Anal. Machine Intell.*, vol. 18, Apr. 1996.

[39] G. Malandin, G. Bertrand, and N. Ayache, "Topological segmentation of discrete surfaces," in *Int. J. Comput. Vision*, vol. 10, no. 2, pp. 183–197, 1993.

[40] M. Kass, A. Witkin, and D. Terzopoulos, "Snakes: Active contour models," *Int. J. Comput. Vision*, vol. 1, no. 4, pp. 321–331, 1988.

[41] F. Leitner, I. Marque, S. Lavallée, and P. Cinquin, "Dynamic segmentation: Finding the edge with snake-splines," in *Proc. Int. Conf. Curves Surfaces*, 1990, pp. 279–284.

[42] G. Borgefors, "Distance transformation in arbitrary dimensions," *Comput. Vision, Graph. Image Processing*, vol. 27, pp. 321–345, 1984.

[43] D. MacDonald, "MNI-display: Program for display and segmentation of surfaces and volumes McConnell Brain Imaging Center MNI, Tech. Rep. 199. Available http://www.bic.mni.mcgill.ca/software/Display/Display.html.

[44] R. Kwan, A. C. Evans, and G. B. Pike, "An extensible MRI simulator for post-processing evaluation," in *Proc. 4th Int. Conf. Visualization Biomedical Computing (VBC)*, Hamburg, Germany, Sept. 1996, pp. 135–140.

[45] D. L. Collins, A. P. Zijdenbos, V. Kollokian, J. G. Sled, N. J. Kabani, C. J. Holmes, and A. C. Evans, "Design and construction of a realistic digital brain phantom," *IEEE Trans. Med. Imag.*, vol. 17, pp. 463–468, June 1998.

[46] A. C. Evans, D. L. Collins, C. Holmes, T. Paus, D. MacDonald, A. Zijdenbos, A. Toga, P. Fox, J. Lancaster, and J. Mazziota, "A 3D probabilistic atlas of normal human neuroanatomy," *Human Brain Mapping*, vol. 4, p. S349, 1997.

[47] Z. Caramanos, R. Venugopal, D. L. Collins, D. MacDonald, A. C. Evans, and M. Petrides, "Human brain sulcal anatomy: An MRI-based study," *Human Brain Mapping*, vol. 4, p. S350, 1997.